Enhancement of Ethanol Vapor Sensing of TiO_2 Nanobelts by Surface Engineering

Peiguang Hu,[†] Guojun Du,[†] Weijia Zhou,[†] Jingjie Cui,[†] Jianjian Lin,[†] Hong Liu,*[,†] Duo Liu,[†] Jiyang Wang,[†] and Shaowei Chen[‡]

State Key Laboratory of Crystal Materials, Center of Bio & Micro/Nano Functional Materials, Shandong University, 27 Shandanan Road, Jinan 250100, P.R. China, and Department of Chemistry and Biochemistry, University of California, 1156 High Street, Santa Cruz, California 95064, United States

ABSTRACT TiO_2 nanobelts were prepared by a hydrothermal process, and the structures were manipulated by surface engineering, including surface coarsening by an acid-corrosion procedure and formation of Ag−TiO_2 heterostuctures on TiO_2 nanobelts surface by photoreduction. Their performance in the detection of ethanol vapor was then examined and compared by electrical conductivity measurements at varied temperatures. Of the sensors based on the four nanobelt samples (TiO_2 nanobelts, Ag−TiO_2 nanobelts, surface-coarsened TiO_2 nanobelts, and surface-coarsened Ag−TiO_2 nanobelts), they all displayed improved sensitivity, selectivity, and short response times for ethanol vapor detection, in comparison with sensors based on other oxide nanostructures. Importantly, the formation of Ag−TiO_2 heterostuctures on TiO_2 nanobelts surface and surface coarsening of TiO_2 nanobelts were found to lead to apparent further enhancement of the sensors sensitivity, as well as a decrease of the optimal working temperature. That is, within the present experimental context, the vapor sensor based on surface-coarsened Ag−TiO_2 composite nanobelts exhibited the best performance. The sensing mechanism was interpreted on the basis of the surface depletion model, and the improvement by oxide surface engineering was accounted for by the chemical sensitization mechanism. This work provided a practical approach to the enhancement of gas sensing performance by one-dimensional oxide nanomaterials.

KEYWORDS: nanoscale Ag-TiO_2 heterostructure • hydrothermal method • surface coarsening • photoreduction • gas sensor

1. INTRODUCTION

Ethanol vapor sensors have been widely used in a wide range of areas, such as chemical, biomedical, and food industries, wine-quality monitoring, and breath analysis (1, 2). In these applications, it is desired that the ethanol vapor sensors exhibit features, such as high sensitivity, high selectivity, high stability, low working temperature, short response and recovery times, etc. Therefore, a great deal of research effort has been devoted to the development of functional materials that may be exploited for the construction of high-performance ethanol vapor sensors. Among these, one-dimensional metal-oxide nanostructures have attracted particular attention, primarily because of their unique physical and chemical properties that arise from the large band gap energy, interesting surface chemistry, as well as high surface to volume ratio. In fact, a variety of 1-D metal oxide nanostructures (1, 3−5) have so far been designed and prepared and have shown good ethanol sensing characteristics. Yet most of these earlier studies were focused on ZnO (6−10), SnO_2 (11−15), V_2O_5 (16), ZrO_2 (17), CuO (18), and WO_3 (19), where their practical applications in high-performance ethanol vapor sensing are impeded by the challenges in mass preparation of these 1-D functional nanostructures. Furthermore, the performance of some of the ethanol vapor sensors (e.g., those based on ZnO nanostructures) may be compromised by the structural instability upon exposure to even a small amount of water (e.g., moisture in an ambient atmosphere) (20).

TiO_2 is a unique functional material used in many areas (21), such as photocatalysis (22−25), solar cell (26−29), electrochemistry (30−33), biology (34−36), and gas sensors (37−39). Significantly, TiO_2 is of lower cost, nontoxicity, and high chemical stability in comparison with other metal oxides such as SnO_2 and ZnO that have been commonly studied as ethanol vapor sensing materials. Previously, TiO_2 nanostructures in the forms of thin films (40, 41), nanotubes (42), and nanowires (43), have been examined as ethanol sensing materials, and the results suggest that TiO_2 1-D nanostructures are remarkable candidates for ethanol vapor sensing. However, in these earlier studies, the sensing performance was found to be limited by several drawbacks, such as low sensitivity, high working temperature (which may result from the low surface area and poor surface structure), and complicated preparation process, etc. It thus remains a great challenge to develop new TiO_2 1-D nanostructures for ethanol vapor sensing with low cost, high sensitivity, high reliability, low working temperature, short response time, and easy preparation process.

Toward this end, TiO_2 nanobelts represent a unique structural building block in several areas (44−46) and should play an important role in ethanol vapor sensing. TiO_2 nanobelts are 1-D nanostructures with the length of several tens of micrometers, width of more than 100 nm, and

* To whom correspondence should be addressed. E-mail: hongliu@sdu.edu.cn.

Received for review August 7, 2010 and accepted October 14, 2010

[†] Shandong University.

[‡] University of California.

DOI: 10.1021/am100707h

thickness of 20−50 nm. TiO_2 nanobelts can be mass-produced by a simple hydrothermal method followed by an acid exchange and calcination process without any capping agent or surfactant (44). Importantly, the gas sensing performance of the TiO_2 nanobelts may be further improved by surface engineering. Experimentally, the effective surface area may be increased by chemical treatments of TiO_2 nanobelts that lead to surface coarsening and the formation of surface defects (47). In addition, the deposition of metal nanoparticles such as Au, Pd, Pt, etc., onto nanostructures (48−50) has been demonstrated to improve the physical and chemical performance of those nanostructures, and accordingly as a consequence of the modulation of the oxide surface energy band structure and the recombination dynamics of photogenerated electrons and holes, the decoration of 1-D metal oxide nanostructures by metal nanoparticles was also found to be able to further enhance the photoelectronic and sensing properties of 1-D metal oxide nanostructures (45, 46, 51−55).

In this paper, TiO_2 nanobelts were synthesized by a hydrothermal method (44), and the structures were manipulated by acid corrosion for surface coarsening as well as deposition of Ag nanoparticles onto the oxide surface for the formation of nanoscale Ag−TiO_2 heterostructures (56). Both of these surface engineering procedures were found to markedly enhance the gas sensing performance toward ethanol.

2. EXPERIMENTAL SECTION

All chemicals used were of analytical grade and were used without further purification. Solutions were freshly prepared with deionized water. Commercial TiO_2 powder (P25, Degussa) was purchased from standard sources and used as received. Analytical reagents of $AgNO_3$, NaOH, HCl (12 M), and H_2SO_4 (18 M) were all purchased from Sinopharm Chemical Reagents Co. Ltd. and were used without further treatment.

2.1. Preparation of TiO_2 Nanobelts. TiO_2 nanobelts were prepared via an alkaline hydrothermal process by using commercial TiO_2 powders as the precursor. The synthetic procedure has been detailed elsewhere (44). Briefly, 0.1 g of P25 powder was dispersed in 20 mL of a 10 M NaOH aqueous solution. After it was stirred magnetically for 10 min, the solution was transferred into a 25 mL Teflon-lined stainless steel autoclave, heated at 200 °C for 48 h, and cooled down to room temperature in air. The products were washed several times with deionized water in a filtration process. Subsequently, the wet powders were dispersed into a 0.1 M HCl aqueous solution for 24 h under slow magnetic stirring and washed thoroughly with deionized water to obtain $H_2Ti_3O_7$ nanobelts, which were then thermally annealed at 600 °C for 1 h to afford crystalline TiO_2 nanobelts.

2.2. Preparation of Surface-Coarsened TiO_2 Nanobelts. Surface-coarsened TiO_2 nanobelts were prepared by an acid-assisted hydrothermal method. Briefly, 0.3 g of $H_2Ti_3O_7$ nanobelts were added into 20 mL of a 0.02 M H_2SO_4 aqueous solution under magnetic stirring. The solution was transferred into a Teflon-lined stainless steel autoclave, heated at 100 °C for 12 h, and cooled to room temperature in air. The wet powder was then washed thoroughly with deionized water, and annealed at 600 °C for 1 h to obtain surface-coarsened TiO_2 nanobelts.

2.3. Preparation of Ag−TiO_2 and Surface-Coarsened Ag−TiO_2 Composite Nanobelts. Ag−TiO_2 and surface-coarsened Ag−TiO_2 composite nanobelts were both synthesized by a photocatalytic reduction method (56) based on TiO_2 nanobelts and surface-coarsened TiO_2 nanobelts obtained from sections 2.1 and 2.2, respectively. In a typical process, 20 mg of TiO_2 or surface-coarsened TiO_2 nanobelts were dispersed into 10 mL of a 0.1 M $AgNO_3$ ethanol solution. The solution was then illuminated with a 20 W ultraviolet lamp under magnetic agitation. The illumination time was 1.5 min and the distance from the lamp to the liquid surface was 10 cm.

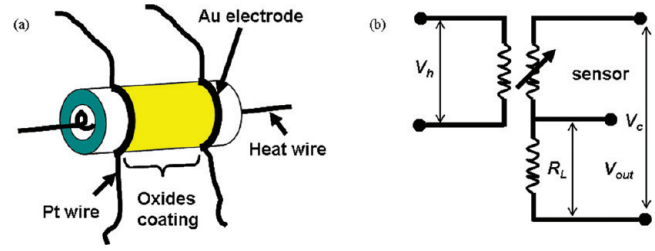

FIGURE 1. Schematics of (a) the ethanol gas sensors and (b) the corresponding equivalent circuit.

2.4. Characterization. X-ray powder diffraction (XRD) patterns were recorded with a Bruker D8 Advance powder X-ray diffractometer with Cu Kα ($\lambda = 0.15406$ nm) radiation. Scanning electron microscopy (SEM) images were acquired using a Hitachi S-4800 electron microscope. Transmission electron microscopy (TEM) images were acquired with a JEM-100CX Π electron microscope. High-resolution TEM images were acquired with a JEOL JEM 2100 electron microscope. All experiments were carried out at room temperature.

2.5. Ethanol Vapor Sensing. The schematic of the ethanol vapor sensors is depicted in Figure 1a. TiO_2 nanobelts, surface-coarsened TiO_2 nanobelts, Ag−TiO_2 nanobelts, or surface-coarsened Ag−TiO_2 nanobelts were used as the sensing materials. The nanobelts were mixed with a calculated amount of water to prepare slurry, which was then coated directly onto the outer surface of a ceramic tube and dried in air, followed by calcination at 400 °C for 48 h. The thickness of the as-prepared films are about 40 μm. (Figures S5 and S6, Supporting Information) Two Au wires were inlaid onto the ceramic tube as electrodes and connected to two Pt wires to quantify the film conductance upon exposure to varied chemical environments. Temperature control was achieved by inserting a resistive heating wire into the ceramic tube.

Vapor detection was carried out with a WS-30A gas sensing system (Zhengzhou Winsen Electronics Technology Co. Ltd., P. R. China) by using a static state gas distribution method. For ethanol detection, an ethanol-air mixed gas was prepared by injecting a certain volume of liquid ethanol into the test chamber on a heating platform where the evaporation of ethanol was aided by two small electric fans.

The sensing electrical circuit is shown in Figure 1b, and the electrical resistance of the sensors in air or in ethanol−air mixed gas is evaluated by $R = [R_L(V_c - V_{out})]/V_{out}$, where R is the sensor resistance, R_L is the load resistance, V_c is the total loop voltage applied to the sensor electrical circuit, and V_{out} is the output voltage across the load resistor. The sensors sensitivity (S) is defined as $S = R_a/R_g$ (13), where R_a is the sensor resistance measured in air with the relative humidity of ~20% and R_g is the resistance measured upon exposure to an ethanol−air mixed gas. The response/recovery time is defined as the time required to reach 90% of the total change of the voltage (V_{out}). V_h is the heater voltage.

3. RESULTS AND DISCUSSION

3.1. Structural Characterizations. The structures of the gas sensing materials, including TiO_2 nanobelts, Ag−TiO_2 nanobelts, surface-coarsened TiO_2 nanobelts, and surface-coarsened Ag−TiO_2 nanobelts, were first characterized by (HR)TEM and SEM measurements. Figure 2 depicts

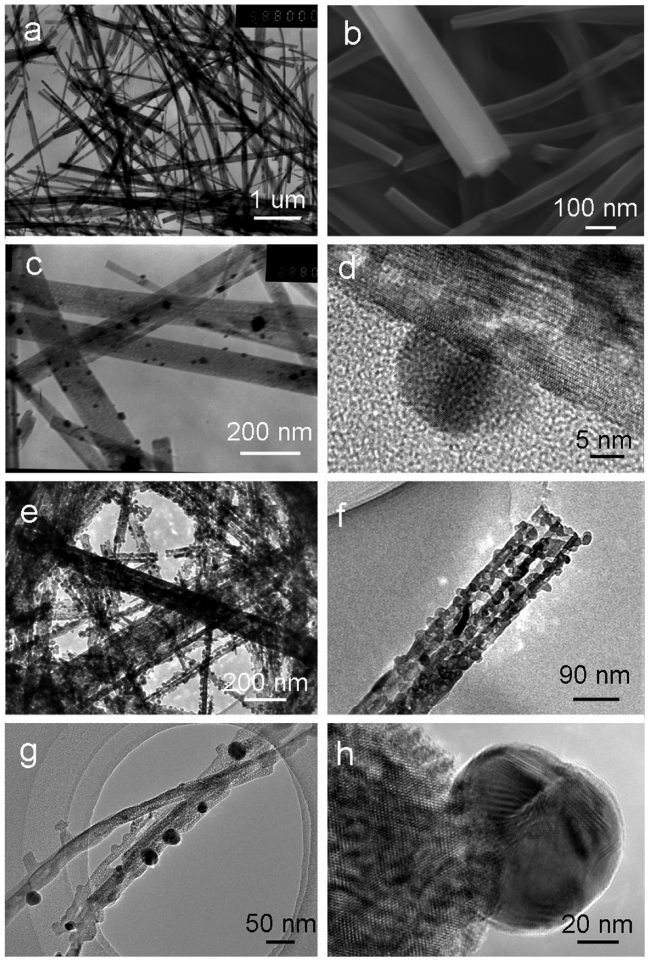

FIGURE 2. Representative (a) TEM and (b) SEM micrographs of TiO_2 nanobelts, (c) Ag−TiO_2 nanobelts, and (HR)TEM micrographs of (d) Ag−TiO_2 nanobelts, (e, f) surface-coarsened TiO_2 nanobelts, and (g, h) surface-coarsened Ag−TiO_2 nanobelts.

the representative (HR)TEM and SEM micrographs of these nanobelt samples. From panels a and b, it can be seen that the TiO_2 nanobelts are 100−150 nm in width, about 50 nm in thickness, and several tens of micrometers in length with a very smooth surface. The (HR)TEM micrographs of Ag−TiO_2 composite nanobelts are shown in panels c and d, where Ag nanoparticles exhibiting a dark contrast can be found to be deposited onto the smooth and crystalline surface of TiO_2 nanobelts, and the diameter of the Ag nanoparticles ranges from 10 to 30 nm. In addition, the dimensions of the nanobelts, as compared to those in panels a and b, remain virtually unchanged. In particular, from panel d, it can be seen that the Ag nanoparticle is largely hemispherical in shape and in intimate contact with the oxide substrate, suggesting that the nanoparticle is not physically absorbed onto the oxide surface but nucleates and grows from the surface. In fact, a heterostructure between two distinctly different crystalline lattices can be clearly identified at the interface. This is consistent with the formation of Ag nanoparticles by TiO_2 photocatalytic reduction.

The impacts of an acid corrosion treatment on the morphologies of the TiO_2 nanobelts are illustrated in panels e and f, where one can see that the nanobelt surfaces were substantially coarsened. Furthermore, after the acid treatment, the width of these surface-coarsened nanobelts can be found to be around 100 nm, which is somewhat smaller than that of the untreated nanobelts (panels a and b). The fact that the nanobelts now exhibited a highly porous structure with a number of TiO_2 nanoparticles (about 30 nm in diameter) attached on the surface indicates a significant enhancement of the effective oxide surface area, as well as the formation of rampant surface defects that may facilitate adsorption of organic molecules.

The HRTEM images of surface-coarsened Ag−TiO_2 composite nanobelts are shown in panels g and h. From panel g, it can be seen that Ag nanoparticles of 20−30 nm in diameter are successfully assembled on the porous TiO_2 nanobelt surface, and the Ag particles are intimately attached to the protuberances on the nanobelts, again forming well-defined nanoscale heterostructures at the Ag/TiO_2 interface (as highlighted in panel d), similar to that observed in panel c.

Further characterizations were carried out with XRD measurements. From Figure 3, it can be seen that the TiO_2 nanobelts (left panel) mainly consist of anatase crystalline phase, with a small amount of β-TiO_2, whereas surface-coarsened TiO_2 nanobelts (right panel) exhibited a pure anatase crystalline phase. The silver nanoparticles on both nanobelts displayed a cubic lattice structure that is consistent with metallic silver (56).

3.2. Ethanol Vapor Sensing. The performance of the varied nanobelts obtained above for ethanol vapor sensing was then examined by using the test apparatus shown in Figure 1. Experimentally, the sensor conductance was measured upon exposure to an ethanol−air mixed vapor with varied ethanol concentration at controlled temperatures.

Figure 4 (left panels) depicts the representative response/recovery curves at 200 °C of the four ethanol vapor sensors based on TiO_2 nanobelts, Ag−TiO_2 nanobelts, surface-coarsened TiO_2 nanobelts, and surface-coarsened Ag−TiO_2 nanobelts. It can be seen that upon the exposure to ethanol vapor of varied concentrations (from 20 to 500 ppm), all sensors exhibited an apparent increase of V_{out}, and the increase becomes more significant at higher concentrations. For instance, at 20 ppm ethanol vapor, the value of V_{out} is 0.118, 0.112, 0.337, and 0.390 V, respectively; whereas at 500 ppm ethanol vapor, V_{out} increases markedly to 0.540, 0.699, 1.989, and 2.957 V. From these measurements, it can be seen that the sensor performance increases in the order of TiO_2 nanobelts < Ag−TiO_2 nanobelts ≈ surface-coarsened TiO_2 nanobelts < surface-coarsened Ag−TiO_2 nanobelts, suggesting the impacts of surface coarsening and formation of metal−TiO_2 heterostructures on the sensor conductance and detection performance (vide infra, sensing mechanism section). Also, it should be noted that the response/recovery time for all four sensors was found to be 1−2 s, which is comparable to that of SnO_2 nanowires-based sensors (11) but much shorter than that of ZnO nanorods-based sensors (6).

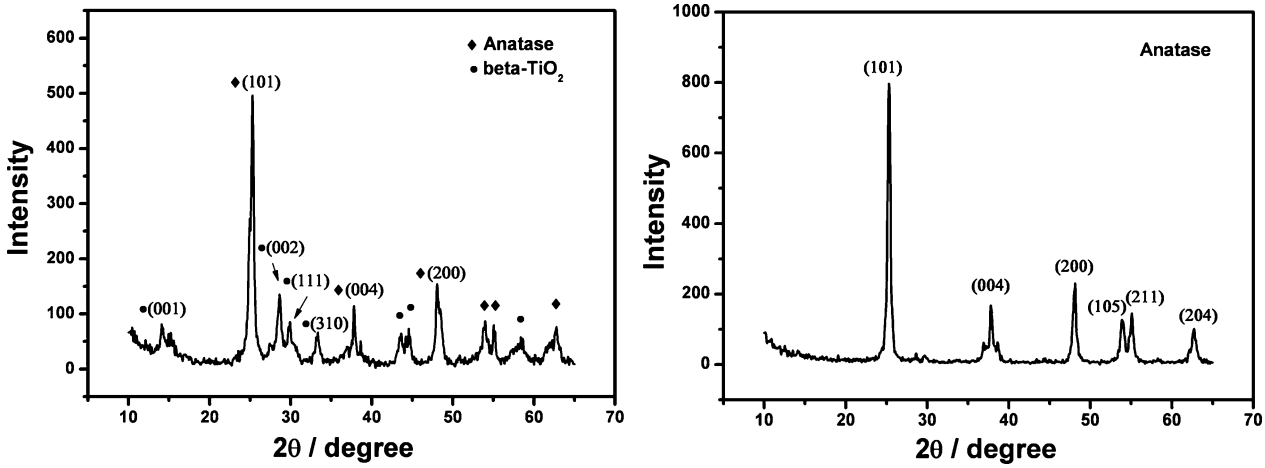

FIGURE 3. XRD patterns of TiO_2 nanobelts (left) and surface-coarsened TiO_2 nanobelts (right).

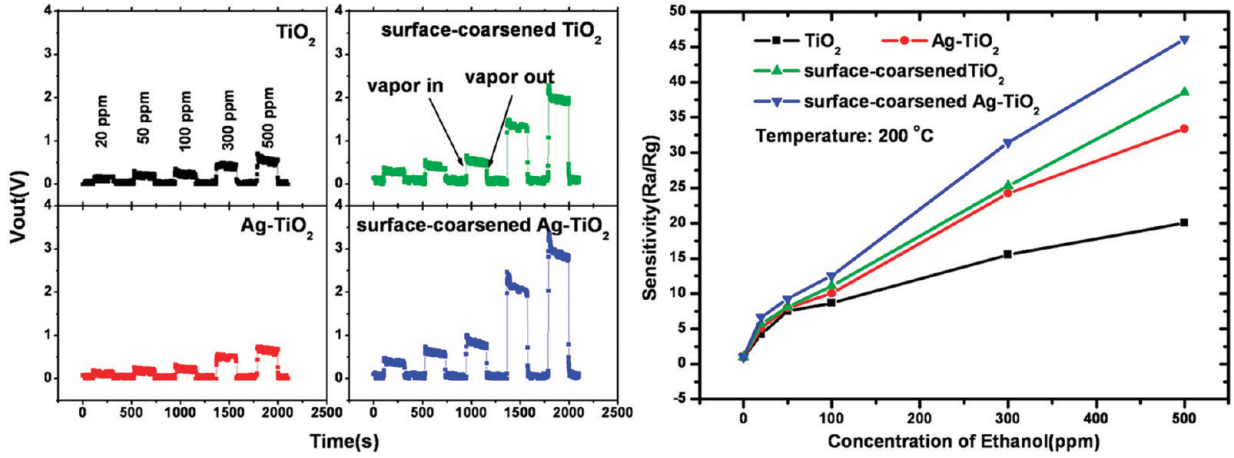

FIGURE 4. (left) Response curves and (right) sensitivity profiles of ethanol vapor sensors based on TiO_2 nanobelts, Ag−TiO_2 nanobelts, surface-coarsened TiO_2 nanobelts, and surface-coarsened Ag−TiO_2 nanobelts upon exposure to different concentrations of ethanol vapor at 200 °C.

The discrepancy of the sensor performance can be further illustrated in the sensitivity (R_a/R_g) profiles depicted in the right panel of Figure 4, where one can see that the sensitivity of all four sensors increases almost linearly with the concentration of ethanol vapor. Notably, at 20 ppm ethanol vapor, the sensitivity can be found to be 4.242, 5.124, 5.732, and 6.659 for the four sensors, respectively; whereas at 500 ppm, it increases drastically to 20.028, 33.410, 38.546, and 46.153. In other words, within the present experimental context, the vapor sensor based on surface-coarsened Ag−TiO_2 nanobelts exhibit the best performance in ethanol vapor detection.

Similar behaviors can be observed at other working temperatures (Figure S1, Supporting Information), and the sensor sensitivity is summarized in Figure 5 which all exhibit peak-shaped dependence on the working temperature with the concentration of ethanol vapor up to 500 ppm. There are at least two aspects that warrant attention here. First, at a specific working temperature and ethanol vapor concentration, coarsening of the nanobelt surface as well as deposition of Ag nanoparticles onto the oxide surface lead to apparent enhancement of the detection sensitivity as compared to sensors based on untreated nanobelts. In fact, the sensor based on surface-coarsened Ag−TiO_2 nanobelts consistently exhibits the best performance among the series in terms of detection sensitivity. Second, the detection sensitivity for sensors based on surface-coarsened (Ag−)TiO_2 nanobelts reaches the maximum at 200 °C (panels c and d), whereas for sensors based on smooth (Ag−)TiO_2 nanobelts, the optimal working temperature is somewhat higher at 250 °C (panels a and b). At lower temperatures (such as 150 °C), the V_{out} signals exhibited a noisy profile with only a fraction of a volt even at 500 ppm ethanol vapor. At higher temperatures (e.g., 250−400 °C), whereas the V_{out} values are somewhat greater, the sensitivity (R_a/R_g) decreases rather substantially with increasing temperature, suggesting increasingly non-negligible background contributions in the conductance measurements.

It should be noted that the electrical conductance (V_{out}) of the vapor sensors remained virtually invariant between before exposure to ethanol vapor and after the test chamber was purged with fresh air, suggesting complete recovery and stability of the TiO_2 nanobelt-based ethanol sensors. Furthermore, the stability and reproducibility of the gas sensors were evaluated by repeating the measurements at least four times under the same experimental conditions (e.g., temperature and ethanol concentration), and the sensors responses in the four measurements under the same condition were almost the same (Figure S2, Supporting Information).

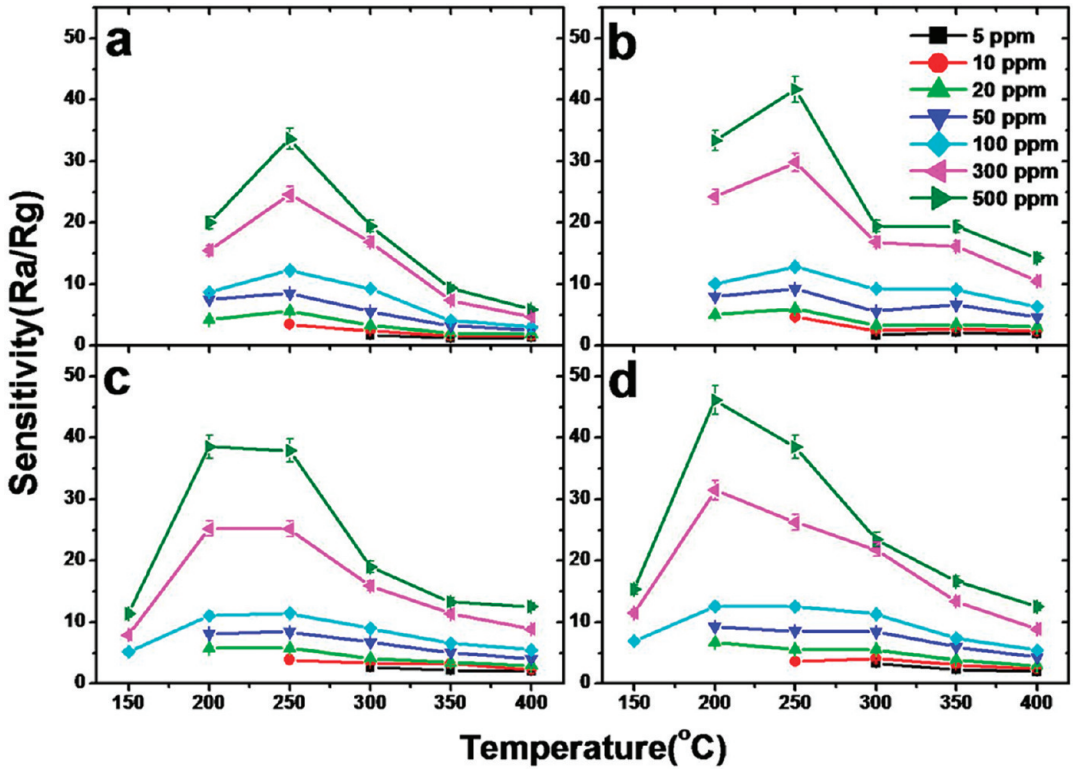

FIGURE 5. Variation of sensitivity (R_a/R_g) with working temperature of the four different kinds of sensors based on (a) TiO_2 nanobelts, (b) Ag−TiO_2 nanobelts, (c) surface-coarsened TiO_2 nanobelts, and (d) surface-coarsened Ag−TiO_2 nanobelts to ethanol vapor of different concentrations.

Table 1. Comparison of Varied Oxide Nanostructures in Ethanol Vapor Sensing

sample	fabrication method	ethanol concentration (ppm)	optimal temp (°C)/ humidity (%)	sensitivity $S = R_a/R_g$	response time/ recovery time (s)	ref
ZnO nanowires	ZnO:Ga/glass as template	500	300/in air	1.754		8
ZnO nanopillars	a two-step solution approach	500	350/in air	33	10/20	9
SnO_2 nanorods	hydrothermal route	100	300/25	13	1/1	11
Pt−TiO_2 nanowires array	naonpatterning process	3500	500/in dry air	7.5	>5/>10	43
TiO_2 nanobelts	hydrothermal method	500	250/20	33.661	1−2	this paper
Ag−TiO_2 nanobelts	hydrothermal method + photocatalytic reduction method	500	250/20	41.709	1−2	this paper
surface-coarsened TiO_2 nanobelts	hydrothermal method	500	200/20	38.546	1−2	this paper
surface-coarsened Ag−TiO_2 nanobelts	hydrothermal method + photocatalytic reduction method	500	200/20	46.153	1−2	this paper

The selectivity of the vapor sensors was then examined by exposing the sensors to other vapors or gas such as CH_3COCH_3, CO, CH_4, and H_2. It was found that all four sensors were totally insensitive to CO, CH_4, and H_2, and exhibited a much lower response to CH_3COCH_3 than to ethanol under any condition (Figures S3 and S4, Supporting Information).

Furthermore, in comparison with other oxide nanostructures, the vapor sensors derivatized from TiO_2 nanobelts all exhibited markedly improved sensitivity (S) in ethanol sensing, which are summarized in Table 1. Additionally, the optimal working temperatures (200−250 °C) were substantially lower those for ZnO nanowires (300 °C) (8), ZnO nanopillars (350 °C) (9), SnO_2 nanorods (300 °C) (11), and Pt−TiO_2 nanowires (500 °C) (43). Also, the nanobelt-based vapor sensors exhibited response and recovery times (only 1−2 s) that are comparable to those of SnO_2 nanorods (11), but significantly shorter than those of ZnO nanopilalrs (9) and Pt−TiO_2 nanowires (43).

3.3. Sensing Mechanism. The experimental observations described above may be accounted for by the surface-depletion model (57), as shown in Figure 6. Similar to other vapor sensors based on metal−oxide semiconductors, the operation of the present sensors is based on manipulation of the electrical resistance (conductance) of the oxide materials that results from the interactions between the target vapor molecules and the active complexes on the oxide surface (6, 12, 57). Mechanistically, as the lower edge of the TiO_2 conduction band is higher than the chemical

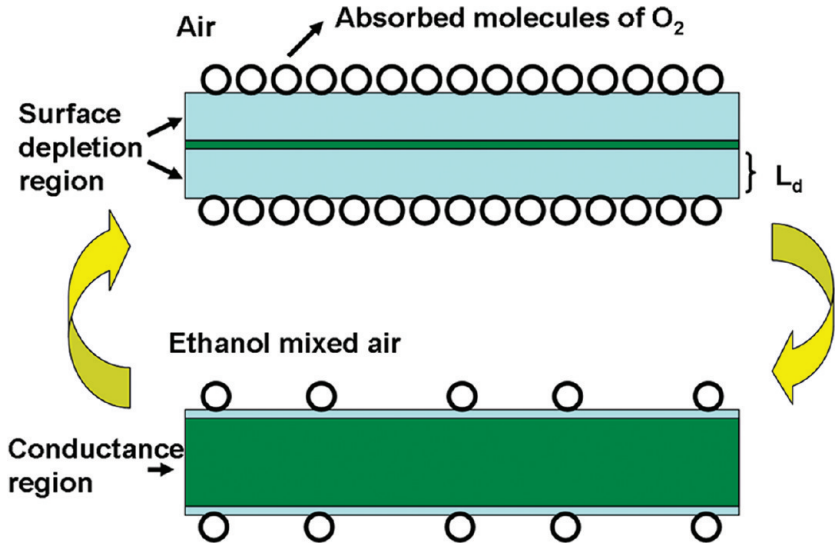

FIGURE 6. Sensing mechanism of TiO_2 nanobelts to ethanol.

potential of O_2 (58), when TiO_2 is exposed to air, O_2 will be adsorbed dissociatively onto the TiO_2 surface, act as effective electron acceptors, capture electrons from the conduction band of TiO_2, and form varied surface active complexes (e.g., superoxo- or peroxo-like species) (59). With the formation of the active complexes, a surface depletion region is created within the oxide matrix (the thickness of this region is denoted as L_d) (60), leading to an increase of the electrical resistance of the TiO_2 layer as a result of the diminishment of charge carrier concentration. In fact, as the thickness of the TiO_2 nanobelts prepared above (Figure 2) is only 20−50 nm (i.e., approximately twice that of L_d), the depletion layer may extend throughout the entire nanobelt, resulting in minimal electrical conductance. However, upon exposure to reducing vapors such as ethanol, effective electron transfer occurs from the vapor molecules to TiO_2 (i.e., ethanol undergoes oxidation reactions), such that the thickness of the surface depletion region decreases accordingly. The increase of charge carrier concentration therefore diminishes the electrical resistance of the TiO_2 film, reflected in the apparent enhancement of the V_{out} response, as observed experimentally (Figure 4).

On the basis of this sensing mechanism, it can be seen that the detection performance will be strongly contingent upon the charge transfer dynamics between the ethanol molecules and the oxide matrix. One effective approach is to deposit metal nanoparticles onto the oxide surface, similar to the Ag−TiO_2 composite nanobelts described above. This is to take advantage of the spillover effects afforded by the metal nanoparticles as a result of the "chemical sensitization" mechanism (51, 61−63). Specifically, because of their large Helmhotz double-layer capacitance, metal nanoparticles are efficient electron sinks. Thus, when supported on reducible oxide surfaces (e.g., TiO_2), partial charge transfer may occur from the oxide metal centers to the metal nanoparticles, leading to the accumulation of negative charges on the metal nanoparticle surface. This may then facilitate the dissociative adsorption of oxygen onto the particle surface and consequently enhance the formation of electron-deficient depletion layer. In fact, such a unique interfacial charge transfer phenomenon has been exploited in the electrocatalytic reduction of oxygen by using metal nanoparticles supported on oxide surfaces (24, 64, 65). Additionally, the deposition of metal nanoparticles onto the oxide surface and hence the intimate interfacial contacts may lead to the formation of structural defects (e.g., Figure 2) and trap states within the oxide band gap. These may serve as the surface active sites for the adsorption of oxygen and alcohol vapor molecules, which is beneficial to the improvement of the ethanol sensing sensitivity, as observed above (Figures 4 and 5).

Experimentally, structural defects can also be created by surface coarsening, as manifested in Figure 2. Both structural defects and the resulting increased effective surface area are anticipated to improve the ethanol sensing performance of TiO_2 nanobelts (66, 67), consistent with the above observations (Figures 4 and 5), where the sensitivity increases and the optimal sensing temperature decreases by about 50 °C with surface-coarsened TiO_2 and Ag−TiO_2 nanobelts as compared to the smooth counterparts.

4. CONCLUSION

In this study, TiO_2 nanobelts were synthesized by a hydrothermal method, and the structures were further manipulated by surface engineering. For instance, the TiO_2 nanobelt surface might be coarsened by an acid-corrosion procedure, and Ag−TiO_2 composite nanoscale heterostructures were produced by depositing silver nanoparticles onto the TiO_2 nanobelt surfaces by photoreduction. The sensing activity of these four nanobelt materials in the detection of ethanol vapor was then examined and compared at controlled temperatures. It was found that surface coarsening and formation of Ag−TiO_2 nanoscale heterostructures (which results from deposition of Ag nanoparticles onto the TiO_2 nanobelts surface) led to apparent improvement in the vapor sensing sensitivity as well as a diminishment of the optimal operation temperature. In fact, within the present experimental context, the vapor sensor based on surface-coars-

ened Ag−TiO_2 composite nanobelts exhibited the best performance. The disparity of the sensing performance was accounted for by the surface depletion model where surface coarsening as well as formation of metal−TiO_2 composite nanoscale heterostructures were exploited as the chemical sensitization mechanism to manipulate the dynamics of interface charge transfer.

Acknowledgment. This research was supported by an NSFC (NSFDYS 50925205, 50872070, 50702031, Grant 50990303, IRG 50721002), and the Program of Introducing Talents of Discipline to Universities in China (111 program No. b06015).

Supporting Information Available: Figures showing response curves, sensitivity profiles, variation of sensitivity, and sectional views of sensor I and II. This information is available free of charge via the Internet at http://pubs.acs.org.

REFERENCES AND NOTES

(1) Kolmakov, A.; Zhang, Y. X.; Cheng, G. S.; Moskovits, M. *Adv. Mater.* **2003**, *15*, 997–1000.
(2) Timmer, B.; Olthuis, W. V. D.; Berg, A. *Sens. Actuators, B* **2005**, *107*, 666–677.
(3) Cui, Y.; Wei, Q. Q.; Park, H. K.; Lieber, C. M. *Science* **2001**, *293*, 1289–1292.
(4) Jia, Y.; He, L. F.; Guo, Z.; Chen, X.; Meng, F. L.; Luo, T.; Li, M. Q.; Liu, J. H. *J. Phys. Chem. C* **2009**, *113*, 9581–9587.
(5) Law, M.; Kind, H.; Messer, B.; Kim, F.; Yang, P. D. *Angew. Chem., Int. Ed.* **2002**, *41*, 2405–2408.
(6) Wan, Q.; Li, Q. H.; Chen, Y. J.; Wang, T. H.; He, X. L.; Li, J. P.; Lin, C. L. *Appl. Phys. Lett.* **2004**, *84*, 3654–3656.
(7) Xu, J. Q.; Chen, Y. P.; Chen, D. Y.; Shen, J. N. *Sens. Actuators, B* **2006**, *113*, 526–531.
(8) Hsueh, T. J.; Hsu, C. L.; Chang, S. J.; Chen, I. C. *Sens. Actuators, B* **2007**, *126*, 473–477.
(9) Bie, L. J.; Yan, X. N.; Yin, J.; Duan, Y. Q.; Yuan, Z. H. *Sens. Actuators, B* **2007**, *126*, 604–608.
(10) Yang, Z.; Li, L. M.; Wan, Q.; Liu, Q. H.; Wang, T. H. *Sens. Actuators, B* **2008**, *135*, 57–60.
(11) Chen, Y. J.; Xue, X. Y.; Wang, Y. G.; Wang, T. H. *Appl. Phys. Lett.* **2005**, *87*, 233503.
(12) Chen, Y. J.; Nie, L.; Xue, X. Y.; Wang, Y. G.; Wang, T. H. *Appl. Phys. Lett.* **2006**, *88*, 083105.
(13) Wan, Q.; Huang, J.; Xie, Z.; Wang, T. H.; Dattoli, E. N.; Lu, W. *Appl. Phys. Lett.* **2008**, *92*, 102101.
(14) Liu, Y.; Koep, E.; Liu, M. L. *Chem. Mater.* **2005**, *17*, 3997–4000.
(15) Gajdoš, Í k, L. *Sens. Actuators, B* **2002**, *81*, 347–350.
(16) Liu, J. F.; Wang, X.; Peng, Q.; Li, Y. D. *Adv. Mater.* **2005**, *17*, 764–767.
(17) Zhang, Z. Y.; Zhang, C.; Zhang, X. *Analyst* **2002**, *127*, 792–796.
(18) Raksa, P.; Gardchareon, A.; Chairuangsri, T.; Mangkorntong, P.; Mangkorntong, N.; Choopun, S. *Ceram. Int.* **2008**, *34*, 823–826.
(19) Ponzoni, A.; Comini, E.; Sberveglieri, G.; Zhou, J.; Deng, S. Z.; Xu, N. S.; Ding, Y.; Wang, Z. L. *Appl. Phys. Lett.* **2006**, *88*, 203101.
(20) Zhou, J.; Xu, N. S.; Wang, Z. L. *Adv. Mater.* **2006**, *18*, 2432–2435.
(21) Zhou, W. J.; Liu, H.; Boughton, R. I.; Du, G. J.; Lin, J. J.; Wang, J. Y.; Liu, D. *J. Mater. Chem.* **2010**, *20*, 5993–6008.
(22) Williams, G.; Seger, B.; Kamat, P. V. *ACS Nano* **2008**, *2*, 1487–1491.
(23) Wu, N. Q.; Wang, J.; Tafen, D. N.; Wang, H.; Zheng, J. G.; Lewis, J. P.; Liu, X. G.; Leonard, S. S.; Manivannan, A. *J. Am. Chem. Soc.* **2010**, *132*, 6679–6685.
(24) Linsebigler, A. L.; Lu, G. Q.; Yates, J. T., Jr. *Chem. Rev.* **1995**, *95*, 735–758.
(25) Osterloh, F. E. *Chem. Rev.* **2008**, *20*, 35–54.
(26) Bach, U.; Lupo, D.; Comte, P.; Moser, J. E.; Weissõrtel, F.; Salbeck, J.; Spreitzer, H.; Grãtzel, M. *Nature* **1998**, *395*, 583–585.
(27) O'Regan, B.; Grãtzel, M. *Nature* **1991**, *385*, 737–740.
(28) Shankar, K.; Feng, X. J.; Grimes, C. A. *ACS Nano* **2009**, *3*, 788–794.
(29) Bang, J. H.; Kamat, P. V. *ACS Nano* **2009**, *3*, 1467–1476.
(30) Guo, Y. G.; Hu, Y. S.; Sigle, W.; Maier, J. *Adv. Mater.* **2007**, *19*, 2087–2091.
(31) Hu, Y. S.; Kienle, L.; Guo, Y. G.; Maier, J. *Adv. Mater.* **2006**, *18*, 1421–1426.
(32) Kim, S. W.; Han, T. H.; Kim, J.; Gwon, H.; Moon, H. S.; Kang, S. W.; Kim, S. O.; Kang, K. *ACS Nano* **2009**, *3*, 1085–1090.
(33) Meekins, B. H.; Kamat, P. V. *ACS Nano* **2009**, *3*, 3437–3446.
(34) Paunesku, T.; Rajh, T.; Wiederrecht, G.; Maser, J.; Vogt, S.; Stojicevic, N.; Protic, M.; Lai, B.; Oryhon, J.; Thurnauer, M.; Woloschak, G. *Nat. Mater.* **2003**, *2*, 343–346.
(35) Magrez, A.; Horváth, L.; Smajda, R.; Salicio, V.; Pasquier, N.; Forró, L.; Schwaller, B. *ACS Nano* **2009**, *3*, 2274–2280.
(36) Mun, K. S.; Alvarez, S. D.; Choi, W. Y.; Sailor, M. J. *ACS Nano* **2010**, *4*, 2070–2076.
(37) Garzella, C.; Comini, E.; Tempesti, E.; Frigeri, C.; Sberveglieri, G. *Sens. Actuators, B* **2000**, *68*, 189–196.
(38) Carotta, M. C.; Ferroni, M.; Gnani, D.; Guidi, V.; Merli, M.; Martinelli, G.; Casale, M. C.; Notaro, M. *Sens. Actuators, B* **1999**, *58*, 310–317.
(39) Radecka, M.; Zakrzewska, K.; Rekas, M. *Sens. Actuators, B* **1998**, *47*, 194–204.
(40) Rella, R.; Spadavecchia, J.; Manera, M. G.; Capone, S.; Taurino, A.; Martino, M.; Caricato, A. P.; Tunno, T. *Sens. Actuators, B* **2007**, *127*, 426–431.
(41) Alessandri, I.; Comini, E.; Bontempi, E.; Faglia, G.; Depero, L. E.; Sberveglieri, G. *Sens. Actuators, B* **2007**, *128*, 312–319.
(42) Seo, M. H.; Yuasa, M.; Kida, T.; Huh, J. S.; Yamazoe, N.; Shimanoe, K. *Procedia Chem.* **2009**, *1*, 192–195.
(43) Francioso, L.; Taurino, A. M.; Forleo, A.; Siciliano, P. *Sens. Actuators, B* **2008**, *130*, 70–76.
(44) Wang, Y. M.; Du, G. J.; Liu, H.; Liu, D.; Qin, S. B.; Wang, N.; Hu, C. G.; Tao, X. T.; Jiao, J.; Wang, J. Y.; Wang, Z. L. *Adv. Funct. Mater.* **2008**, *18*, 1131–1137.
(45) Wang, J.; Tafen, D. N.; Lewis, J. P.; Hong, Z. L.; Manivannan, A.; Zhi, M. J.; Li, M.; Wu, N. Q. *J. Am. Chem. Soc.* **2009**, *131*, 12290–12297.
(46) Zhang, H. Y.; Ji, T. H.; Liu, Y. F.; Cai, J. W. *J. Phys. Chem. C* **2008**, *112*, 8604–8608.
(47) Yang, S. G.; Quan, X.; Li, X. Y.; Fang, N.; Zhang, N.; Zhao, H. M. *J. Environ. Sci. (Beijing, China)* **2005**, *17*, 290–293.
(48) Che, G.; Lakshmi, B. B.; Fisher, E. R.; Martin, C. R. *Nature* **1998**, *393*, 346–349.
(49) Sun, Y. G.; Wang, H. H. *Adv. Mater.* **2007**, *19*, 2818–2823.
(50) Xing, Y. C. *J. Phys. Chem. B* **2004**, *108*, 19255–19259.
(51) Kolmakov, A.; Klenov, D. O.; Lilach, Y.; Stemmer, S.; Moskovits, M. *Nano Lett.* **2005**, *5*, 667–673.
(52) Joshi, R. K.; Kuis, F. E. *Appl. Phys. Lett.* **2006**, *89*, 153116.
(53) Hsueh, T. J.; Chang, S. J. *Appl. Phys. Lett.* **2007**, *91*, 053111.
(54) Jia, L. C.; Cai, W. P.; Wang, H. Q. *Appl. Phys. Lett.* **2010**, *96*, 103115.
(55) Neri, G.; Bonavita, A.; Micali, G.; Donato, N.; Deorsola, F. A.; Mossino, P.; Amato, I.; De Benedetti, B. *Sens. Actuators, B* **2006**, *117*, 196–204.
(56) Wang, Y. M.; Du, G. J.; Liu, H.; Liu, D.; Qin, S. B.; Wang, J. Y.; Tao, X. T.; Jiang, M. H.; Wang, Z. L. *J. Nanosci. Nanotechnol.* **2009**, *9*, 2119–2123.
(57) Feng, P.; Wan, Q.; Wang, T. H. *Appl. Phys. Lett.* **2005**, *87*, 213111.
(58) Nozik, A. J.; Memming, R. *J. Phys. Chem.* **1996**, *100*, 13061–13078.
(59) Li, Q. H.; Liang, Y. X.; Wan, Q.; Wang, T. H. *Appl. Phys. Lett.* **2004**, *85*, 6389–6391.
(60) Kolmakov, A.; Moskovits, M. *Annu. Rev. Mater. Res.* **2004**, *34*, 151–180.
(61) Yamazoe, N.; Kurokawa, Y.; Seiyama, T. *Sens. Actuators* **1983**, *4*, 283–286.
(62) Yamazoe, N. *Sens. Actuators, B* **1991**, *5*, 7–19.
(63) Joshi, R. K.; Kruis, F. E. *Appl. Phys. Lett.* **2006**, *89*, 153116.
(64) Jang, J. S.; Choi, S. H.; Kim, D. H.; Jang, J. W.; Lee, K. S.; Lee, J. S. *J. Phys. Chem. C* **2009**, *113*, 8990–8996.
(65) Xin, B. F.; Jing, L. Q.; Ren, Z. Y.; Wang, B. Q.; Fu, H. G. *J. Phys. Chem. B* **2005**, *109*, 2805–2809.
(66) Huang, H.; Tan, O. K.; Lee, Y. C.; Tran, T. D.; Tse, M. S.; Yao, X. *Appl. Phys. Lett.* **2005**, *87*, 163123.
(67) Chen, Y. J.; Zhu, C. L.; Xiao, G. *Nanotechnology* **2006**, *17*, 4537–4541.

AM100707H